PERGAMON

Journal of Structural Geology 26 (2004) 221–231

JOURNAL OF STRUCTURAL GEOLOGY

www.elsevier.com/locate/jsg

Origin of deformation bands in argillaceous sediments at the toe of the Nankai accretionary prism, southwest Japan

Kohtaro Ujiie[a,*], Alex J. Maltman[b], Mario Sánchez-Gómez[c]

[a]*Institute for Frontier Research on Earth Evolution, Japan Marine Science and Technology Center, 3173-25 Showa-machi, Yokohama 236-0001, Japan*
[b]*Institute of Geography and Earth Sciences, University of Wales, Aberystwyth SY23 3DB, UK*
[c]*Departamento de Geología, Universidad de Jaén, Virgen de la Cabeza 2, 23071 Jaén, Spain*

Received 20 March 2003; received in revised form 30 June 2003; accepted 30 June 2003

Abstract

Deformation bands in argillaceous sediments at the toe of the Nankai accretionary prism are roughly planar, ~1–10 mm thick, bedding-oblique zones. The bands are typically developed as two oppositely dipping sets. A band of one set can be displaced by the slickenlined surface of the oppositely dipping band, showing a reverse slip with respect to a horizontal plane. Deformation bands commonly consist of thinner subbands that are oblique or parallel to the boundaries of the deformation bands. The subbands also display a reverse slip with respect to a horizontal plane, and particles within subbands are oriented perpendicular to the maximum principal stress (σ_1), regardless of the dips of the subbands. Physical property analysis using an X-ray computed tomography scanner demonstrates that porosity reduction in the deformation bands relative to the surrounding undeformed material ranges from 1 to 6%. The deformation bands are compactive shear bands formed under subhorizontal σ_1 associated with northwest-directed plate convergence, and subbands arise from a combination of reverse sense of shear and flattening perpendicular to σ_1, with their geometries producing the S–C aspect observed in sheared clayey sediments or ductile metamorphic shear zones.

Keywords: Deformation bands; X-ray CT scanner; Nankai accretionary prism; Ocean Drilling Program; *JOIDES Resolution*; Site 1174

1. Introduction

The toes of accretionary prisms are regions where deformation of submarine sediments occur by frontal accretion (e.g. Maltman et al., 1993; Ujiie, 1997). Prism toes provide opportunities to examine (1) the influence of plate convergence-related tectonic stresses on poorly consolidated sediments, (2) changes in physical properties associated with accretion-related soft-sediment deformation, and (3) early deformational fabrics of tectonic origin. These early tectonic processes are rarely preserved in on-land ancient accretionary complexes, which tend to record subsequent deformation and various degrees of diagenesis and/or metamorphism.

Roughly planar, 0.5–5 mm wide, microscopic-scale bedding-oblique dark bands typically develop in argillaceous sediments at the toes of accretionary prisms (Fig. 1) and have been called deformation bands (e.g. Maltman, 1998). Deformation bands are exceptionally well developed at the toe of the Nankai accretionary margin, but examples have also been reported from other convergent plate margins such as Chile (Rochford et al., 1995) and Costa Rica (Vannucchi and Tobin, 2000). Previous studies of deformation bands mainly used cores obtained from the Deep Sea Drilling Project (DSDP) and the Ocean Drilling Program (ODP) from convergent plate margins. However, the origin of deformation bands remains poorly understood. For example, Lundberg and Moore (1986) viewed deformation bands as kink bands. By contrast, Karig and Lundberg (1990) considered deformation bands as equivalent to shear fractures that are compatible with a brittle Coulomb criterion. Maltman et al. (1993) described deformation bands as displaying various kink-, ductile shear zone-, and fault-like aspects.

ODP Leg 190 penetrated the toe of the Nankai accretionary prism off Shikoku Island, southwest Japan (Fig. 2a). Here, the Philippine Sea Plate is subducting

* Corresponding author.
E-mail address: ujiiek@jamstec.go.jp (K. Ujiie).

0191-8141/$ - see front matter © 2003 Elsevier Ltd. All rights reserved.
doi:10.1016/j.jsg.2003.06.001

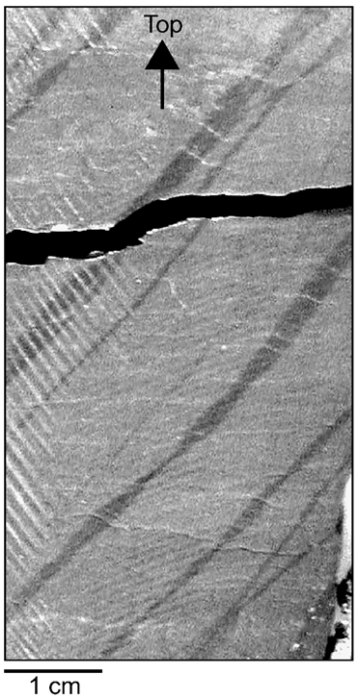

Fig. 1. Photograph of split core showing deformation bands (dark zones) in argillaceous sediments at the toe of the Nankai accretionary prism. Core top is perpendicular to a horizontal plane. Interval 190-1174B-17R-2, 105–112 cm.

beneath southwest Japan at a rate of 4 cm/yr, with the plate motion vector trending northwest (Seno, 1977). Cores recovered from Site 1174 provide an invaluable opportunity to study deformation bands and allow us to compare them with previous results obtained from other convergent plate margins. Site 1174 is located between the deformation front and the frontal thrust, where incipient deformation is expected to occur in the toe of the Nankai accretionary prism (Fig. 2b). This site penetrated the prism protothrust and basal décollement, the underthrust sediments, and reached the oceanic crust. Deformation of the sediments above the décollement is characterized by deformation bands and fractured and brecciated zones, whereas the sediments below the décollement show little deformation (Moore et al., 2001b).

In this paper, detailed core- and optical microscopic-scale observations of deformation bands at Site 1174 are first presented. We then quantitatively address how the physical properties of the soft sediments have changed due to the formation of deformation bands. Based on these results, we present new insights into the origin of deformation bands.

2. Character and internal structure of deformation bands

Deformation bands tend to be observed in clay-rich sediments that lack bioturbation, and range in thickness from ~1 to 10 mm. Fig. 3 shows the variation in dips of bedding and deformation bands with depth in the upper part of Site 1174. Deformation bands are concentrated in the interval between ~218 m below the seafloor (mbsf) and the fault zone at 306 mbsf. The latter horizon is characterized by a 35-cm-thick foliated breccia interpreted to be a backthrust within the prism, which strikes northeast and dips moderately southeastward (Moore et al., 2001a). Thus, deformation bands are concentrated in the hanging wall of this backthrust. Deformation bands have also developed in ash layers at deeper levels: 510 and 590 mbsf, but these are relatively rare. Except for the protothrust zone between 463 and 504 mbsf, bedding dips are mostly less than 20°. By contrast, many of the deformation bands dip between 40 and 70°. The orientation data for the deformation bands were corrected for vertical-axis rotations due to drilling. The corrections to true geographic orientations utilized natural remanent magnetization data collected during Leg 190, and details of the correction method are given in Moore et al. (2001a). The orientations of the deformation bands after corrections are concentrated into two oppositely dipping sets that strike northeast (Fig. 4a). The lesser dihedral angle between the set is 67°, the bisector of which is inclined 10° from vertical toward the northwest (Fig. 4b).

The deformation bands commonly change in width along their length, and rarely occur as widely spaced, parallel-sided planar bands. Typically, the deformation bands are developed as two sets that dip in opposite directions (Fig. 5). One of the bisectors of the dihedral angle is oriented parallel to bedding-parallel fissility. In places, deformation bands (e.g. deformation band A in Fig. 5) are displaced by oppositely dipping deformation bands, showing a reverse sense with respect to the horizontal plane. Displacement along individual bands is small, mostly less than 5 mm. The horizontal fractures, which represent fissile intervals, are deflected by the deformation bands, showing kink-like geometries with a reverse sense. However, the up- and down-stepping of horizontal fractures may be due to linkage of fractures that formed upon unloading of the specimen from depth. Many of the deformation bands consist of thinner and darker subbands that dip 5–20° less steeply than the boundaries of the deformation bands. A reverse sense of shear with respect to a horizontal plane along the less steeply dipping subbands is locally discernible from the displacement of the deformation band boundaries (Fig. 5). Displacement along individual subbands is commonly less than 1 cm. The margins of both the deformation bands and subbands are polished and slickenlined.

The microstructures within the deformation bands were examined using an optical microscope. This standard method is useful for microstructural analysis of porous, fine-grained sediments (Lewis et al., 1997). Since the samples were poorly consolidated and clayey, an improved embedding method employing epoxy resin Quetol 651 (Takizawa et al., 1995) was adopted to reduce as much as possible any disturbance of the original microstructures due

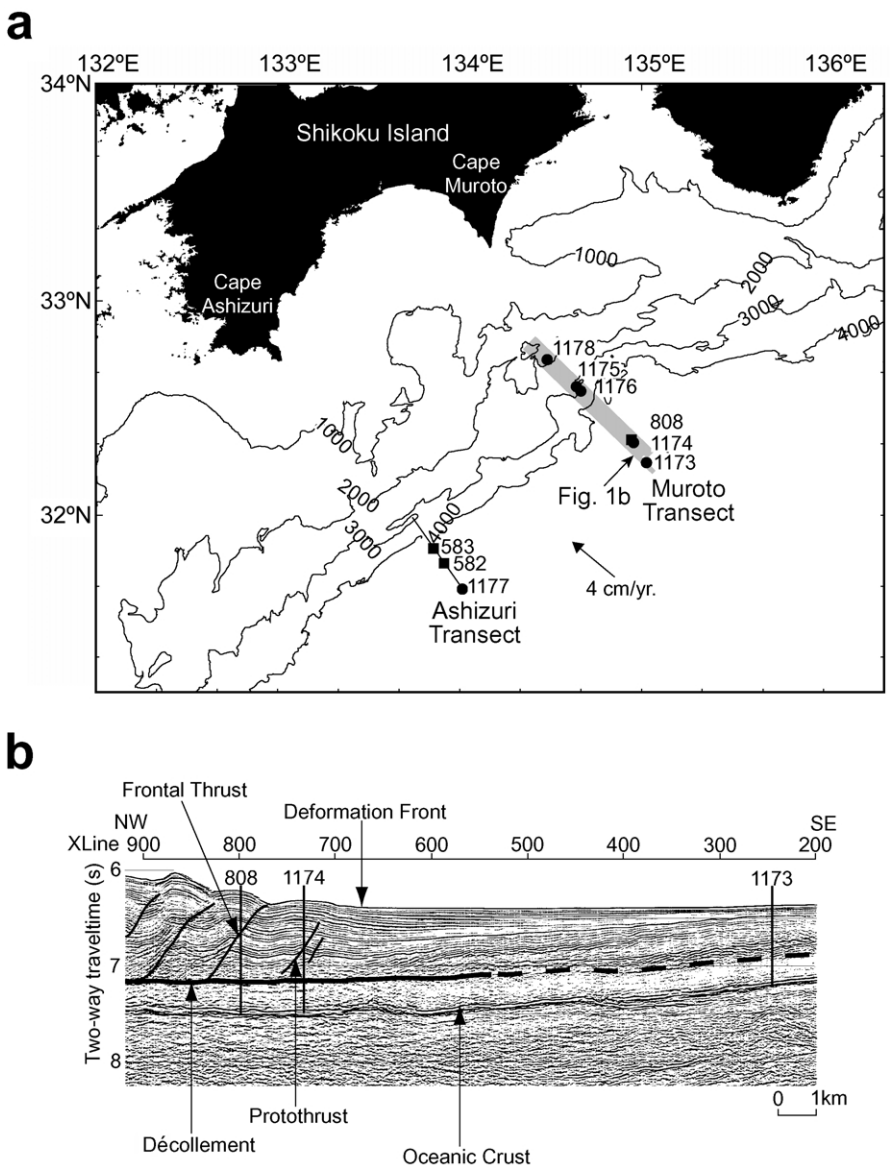

Fig. 2. (a) Location map showing Ocean Drilling Program Leg 190 (solid circles) and previous drilling sites (solid squares) off Shikoku Island, southwest Japan. Arrow indicates the plate convergence vector for the Philippine Sea plate. Deformation bands have been observed at Sites 583, 808 and 1174. (b) Seismic reflection profile through the reference (Site 1173) and prism toe sites (Sites 1174 and 808).

to surface tension effects and shrinkage. Under the optical microscope, the subbands are expressed by bright interference colors, reflecting relatively well-oriented particles (Fig. 6). Particles in the sectors of the deformation bands between subbands display a much less preferred orientation. The less steeply dipping subbands merge with those oriented parallel to the boundaries of the deformation bands (Fig. 6a and b), or terminate at the deformation band boundaries. As in the case of core-scale observations, it is also possible to detect a reverse sense of shear with respect to the horizontal plane along deformation band or less steeply dipping subband (Fig. 6c). Some deformation bands consist of subbands that are subparallel but locally merge with one another.

The reverse sense of shear on the deformation band and subband is more apparent under the optical microscope at high magnifications. Fig. 7a illustrates a close-up of two oppositely dipping sets of subbands that are oriented parallel to the boundaries of the deformation bands. Subband A is displaced by the oppositely dipping subband B, with a reverse sense with respect to the horizontal plane. The orientation of particles within the subbands deviates significantly from that of the compaction related bedding-parallel phyllosilicate fabric (Fig. 7b). Thus, the change in the orientation of particles across the subbands displays a kink-like geometry with a reverse sense. Fig. 8 and Table 1 give an example of the relationship between the external and internal angles of the kink-like subbands in the deformation bands, which was optically determined using polarized light and a quartz interference plate. The external angle is the

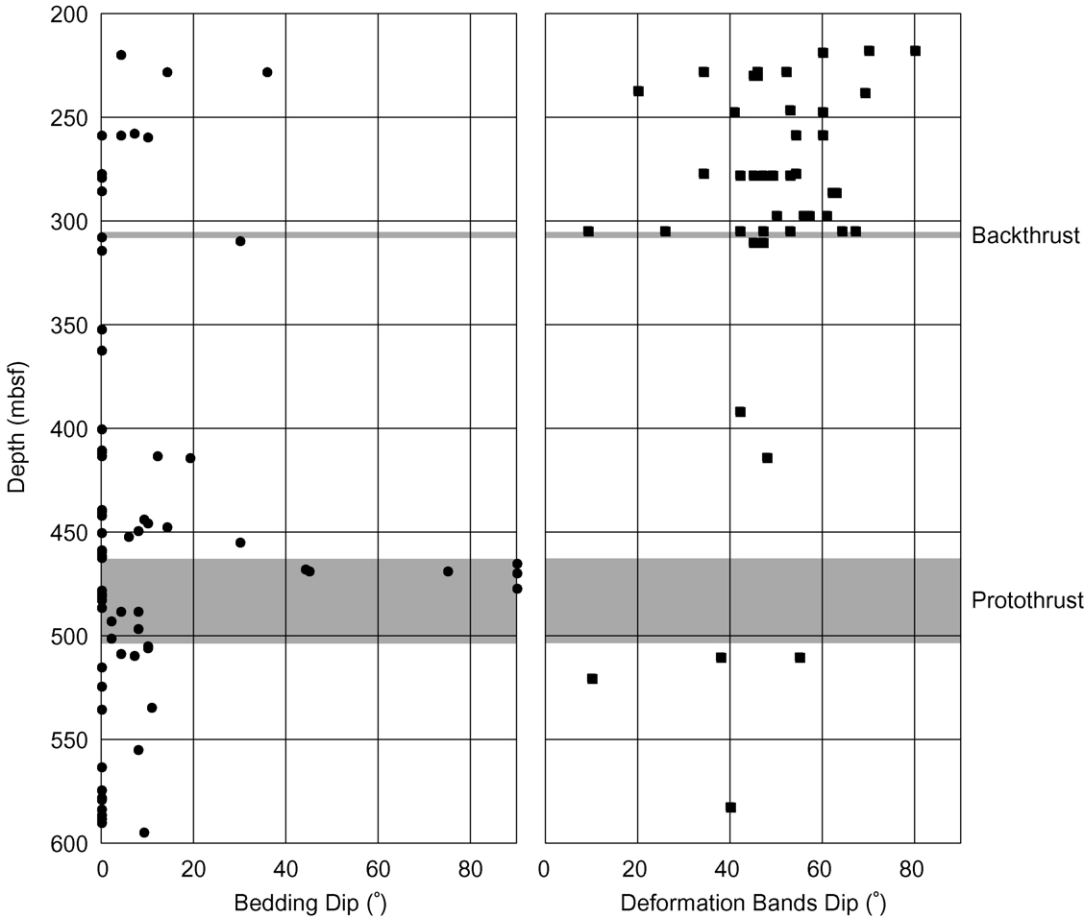

Fig. 3. Distribution of bedding and deformation band dips with depth in the upper part of the accretionary prism at Site 1174.

angle between the bedding-parallel phyllosilicate fabric and the subband, whereas the internal angle indicates the angle between the subband boundary and the internal particles in the subband. The external and internal angles range from 39 to 63° and 38 to 54°, respectively (Fig. 8). The sum of the external and internal angles is approximately 90°, demonstrating that the particles within the subbands are oriented perpendicular to the bedding-parallel phyllosilicate fabric, regardless of the dips of the subbands (Table 1). This result is in contrast to Byrne et al. (1993), who reported consistent external angles (45°) and internal angles that were highly variable (0–45°). Fig. 8 also indicates that most of the

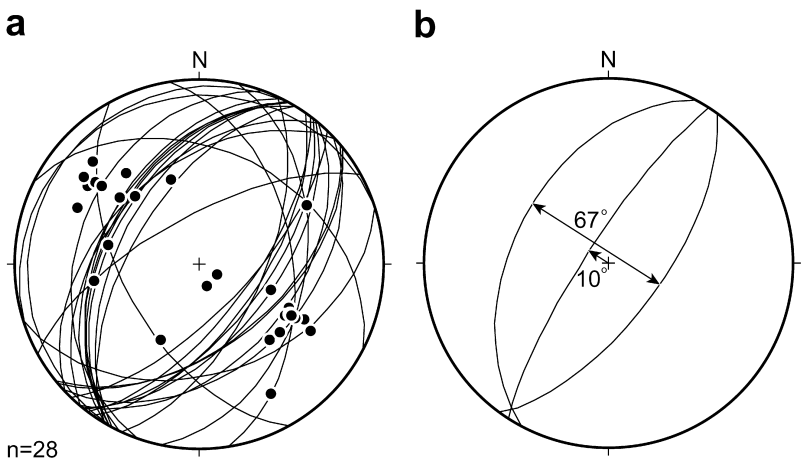

Fig. 4. (a) Lower hemisphere equal-area stereographic projection showing great circles of deformation bands after paleomagnetic reorientation. Poles to corresponding surfaces of deformation bands are also shown. (b) Average of the two sets of deformation bands showing the dihedral angle and the inclination from vertical to the acute bisector.

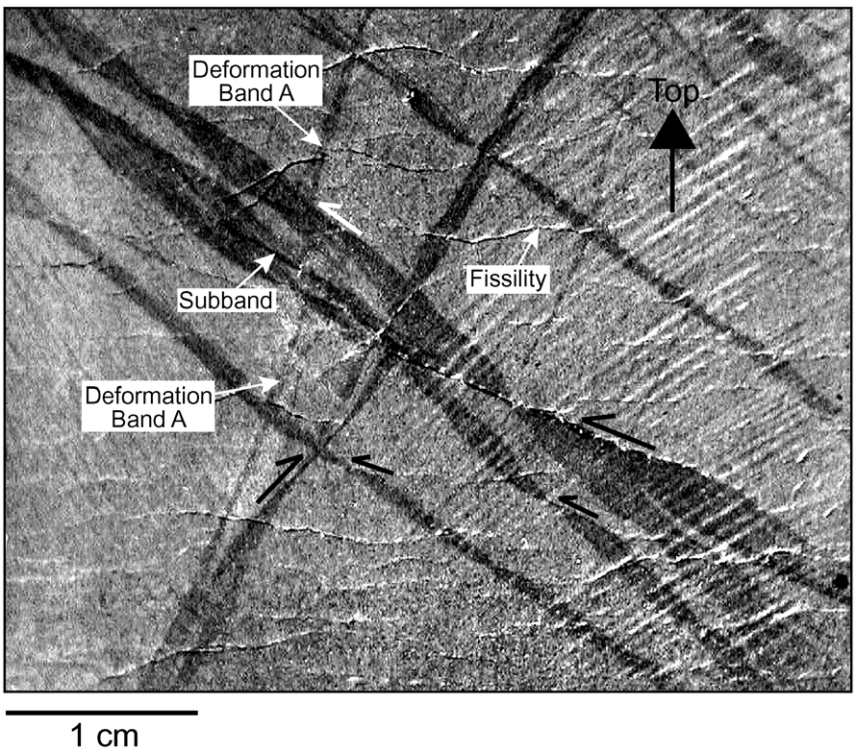

Fig. 5. Photograph of a split core showing two oppositely dipping sets of deformation bands. A white half-arrow and black half-arrows indicate sense of shear along the deformation bands and the less steeply dipping subbands, respectively. See text for further explanation. Core top is perpendicular to a horizontal plane. Interval 190-1174B-15R-2, 20–24 cm.

subbands record a decrease in volume during their development. This result is unusual for typical kink bands, which commonly record an increase in volume during their development (Suppe, 1985).

3. Physical property changes associated with the formation of deformation bands

Quantitative analysis of physical property changes associated with the formation of deformation bands was carried out using X-ray computed tomography (CT). The X-ray CT scanner is a useful tool for the nondestructive, quantitative analysis of the spatial distribution of bulk density or chemical composition (e.g. Anderson et al., 1988; Byrne et al., 1993; Soh et al., 1993). The CT scanner used for the analysis was a HITACHI MEDICO CT-W2000. The imaging conditions were as follows: 120 kV and 100 mA X-ray tube voltage and current, 4.0 s scan time, 1.0 mm slice interval. The number of pixels in a CT image is 512×512 and the size of each pixel is 0.313×0.313 mm^2. CT-W2000 converts X-ray linear absorption coefficients to CT numbers. High CT numbers correspond to bright colors in CT images, indicating relatively high bulk density or a high average atomic number of the material.

The samples for X-ray CT analysis were taken from the mudstones, with an additional sample from an ash layer in which deformation bands were well developed. Mudstones without deformation structures were selected from various depths of Site 1174 and also analyzed as reference samples to correlate with Leg 190 shipboard bulk density data (described later). All samples were kept wet immediately after core recovery, and the CT scans were performed on samples with original fluid saturation. The average CT numbers were obtained from the central part of the samples to avoid the influence of "beam hardening" (Nakano et al., 2000). The domain for calculation of the average CT number in reference samples and the undeformed material near to deformation bands ranged from 108 to 900 pixels, while that in deformation bands was extremely limited: consistently 4 pixels.

Table 1
Measured external angle, internal angle, and sum of external and internal angles of kink-like subbands in deformation bands

External angle	Internal angle	Sum of external and internal angles
54	44	98
46	44	90
45	39	84
54	44	98
41	39	80
50	43	93
54	49	103
54	38	92
44	42	86
39	54	93
63	50	113

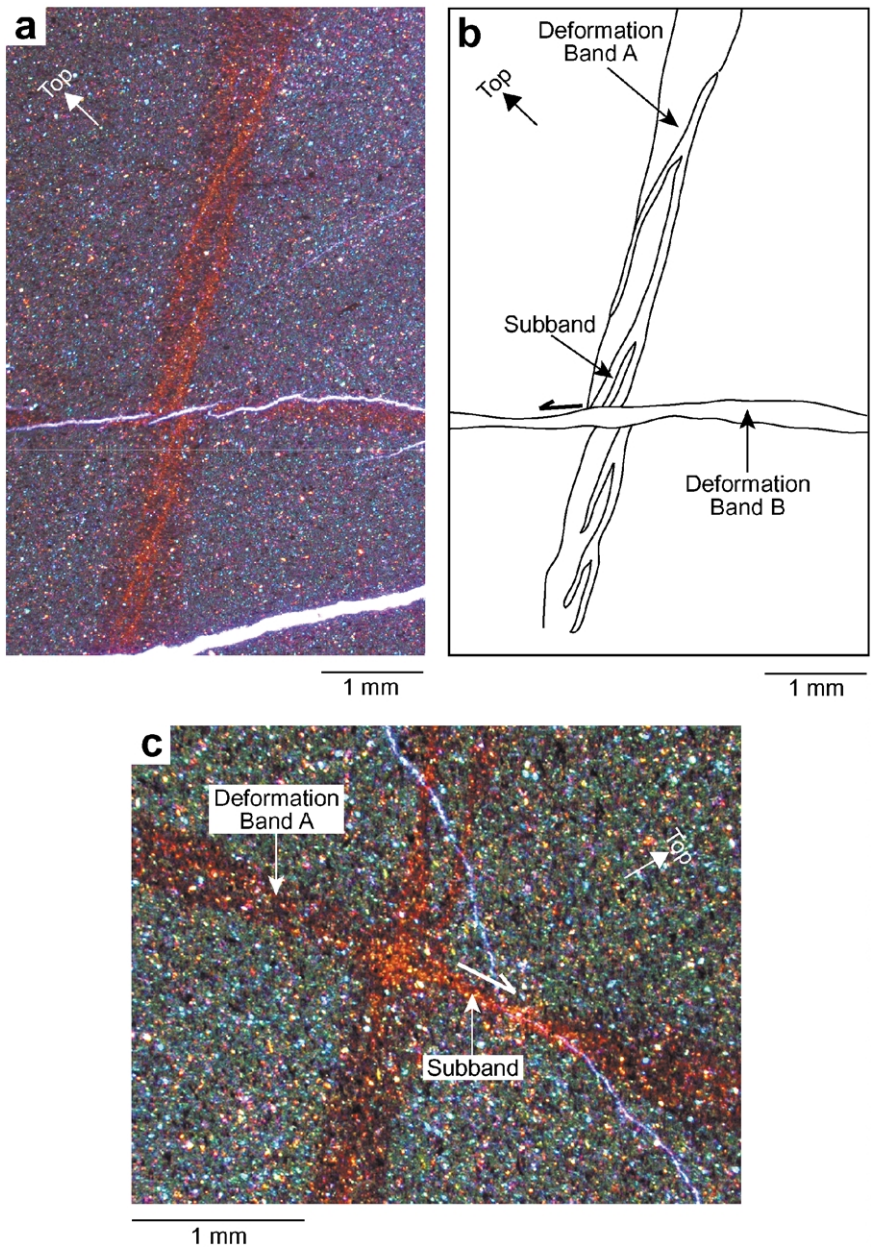

Fig. 6. Microscopic appearance of deformation bands. Note that the core top is perpendicular to a horizontal plane but is inclined in this figure to emphasize the bright interference colors of the subbands. (a) Photomicrograph of deformation bands from sample 190-1174B-12R-1, 78–81 cm. Crossed nicols with an interference plate. (b) Drawing of (a). Note that the subband within deformation band A is subtly displaced by deformation band B, showing a reverse sense with respect to a horizontal plane. Half-arrow indicates sense of shear. (c) Photomicrograph of two oppositely dipping sets of deformation bands. Sample 190-1174B-12R-1, 78–81 cm. Crossed nicols with an interference plate. The boundaries of deformation band A are subtly displaced by the less steeply dipping subband, showing a reverse sense with respect to a horizontal plane. Half-arrow indicates sense of shear.

The deformation bands are expressed as bright bands or seams on the CT images with relatively high CT numbers, suggesting that the bands are either more dense than the surrounding material or rich in elements with atomic numbers higher (e.g. Fe) than the surrounding undeformed material (Fig. 9). Microprobe study indicates that there is no increase in elements of high atomic number within the deformation bands (Ujiie and Nakano, 2002). Thus, the CT images of the deformation bands indicate a relatively high bulk density within the bands.

To quantify the bulk density changes during the development of the deformation bands, we first correlated the average CT numbers of reference samples with Leg 190 shipboard bulk density data that were collected less than 50 cm from the reference samples (Fig. 10). A similar correlation was also performed by Soh et al. (1993). The results of the correlation led to the following equation:

$$\rho = 0.96 + 6.7 \times 10^{-4} \times CT_{\mathrm{N}} \ (R = 0.92) \qquad (1)$$

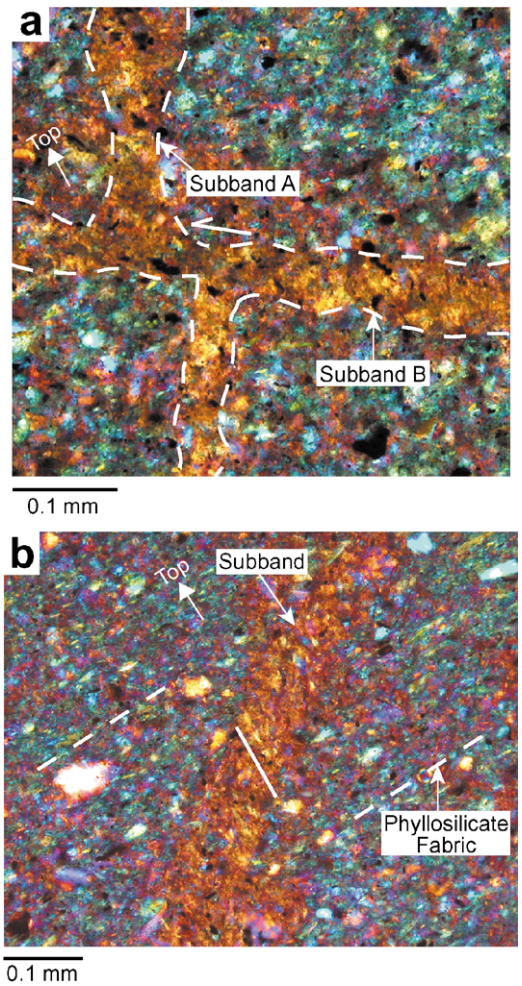

Fig. 7. Microscopic appearance of subbands within deformation bands. Crossed nicols with an interference plate. Note that core top is perpendicular to a horizontal plane but is inclined in this figure to emphasize the bright interference colors of the subbands. (a) Photomicrograph of two oppositely dipping sets of subbands from sample 190-1174B-12R-1, 78–81 cm. Half-arrow indicates sense of shear. (b) Photomicrograph of subband from sample 190-1174B-15R-CC, 18–24 cm. The continuous white line indicates the orientation of particles within the subband, optically determined using polarized light and a quartz interference plate.

where ρ and CT_N are Leg 190 shipboard bulk density and average CT number of the reference samples, respectively. We then used Eq. (1) to calculate the bulk densities of the deformation bands and the surrounding undeformed material from their average CT numbers. As shown in Table 2, the increase in bulk density in the deformation bands relative to the surrounding undeformed material ranges from 0.02 to 0.10 g/cm^3.

Based on microscopic-scale observations, the increased bulk density in the deformation bands appears to be related to porosity reduction. Thus, under fluid saturated conditions, the bulk density of the deformation bands (ρ_d) and the surrounding undeformed material (ρ_u) can be expressed using the porosities of the deformation bands (η_d) and of the surrounding undeformed material (η_u):

$$\rho_d = \eta_d\rho_f + (1 - \eta_d)\rho_g \quad (2)$$

$$\rho_u = \eta_u\rho_f + (1 - \eta_u)\rho_g \quad (3)$$

where ρ_f, and ρ_g, are fluid and grain density, respectively. From Eqs. (2) and (3), the porosity reduction associated with the deformation bands can be expressed as follows:

$$\eta_d - \eta_u = \frac{\rho_d - \rho_u}{\rho_f - \rho_g} \quad (4)$$

We used the density of seawater for ρ_f, (1.024 g/cm^3); Leg 190 shipboard grain density data, collected from less than a few 10 cm from the samples with deformation bands, were used for ρ_g; and ρ_d and ρ_u were determined using Eq. (1). The porosity reduction in the deformation bands relative to the surrounding undeformed material ranges from -0.01 to -0.06 (Table 2). The relatively small changes in porosity may reflect uncertainties in the correlation between the average CT number of the reference samples and the Leg 190 shipboard bulk density data. In the ash layer, the differences in bulk density and porosity between the deformation bands and the surrounding undeformed material was generally small compared with the differences in the mudstones (Table 2). This suggests a lithological influence on the physical property changes associated with the formation of the deformation bands. Overall, the marked bulk density increase and porosity reduction in the deformation bands relative to the surrounding undeformed material, as well as the bright CT images of bands with relatively high CT numbers, strongly suggest that the deformation bands are zones of porosity reduction.

4. Discussion

A number of observations provide information on stress orientation during development of the deformation bands. These observations include: (1) the orientations of the deformation bands are concentrated into two oppositely dipping sets (Fig. 4); (2) the deformation bands and subbands commonly show reverse displacements with respect to a horizontal plane (Figs. 5–7a); and (3) one of the bisectors of the dihedral angle is commonly oriented parallel to the subhorizontal bedding-parallel phyllosilicate fabric that defines fissility. All of these features suggest that the maximum principal stress (σ_1) was parallel to bedding during the development of the deformation bands, bisecting the obtuse angle between the two oppositely dipping sets (Fig. 4). Thus, σ_1 was considered to be subhorizontal and was parallel to the plate convergence vector that trends northwest (Seno, 1977; Byrne et al., 1993). The concentration of deformation bands in the hanging wall of the backthrust at Site 1174 (Fig. 3) and around the frontal thrust at Site 808, located ~2 km landward of Site 1174 (Maltman

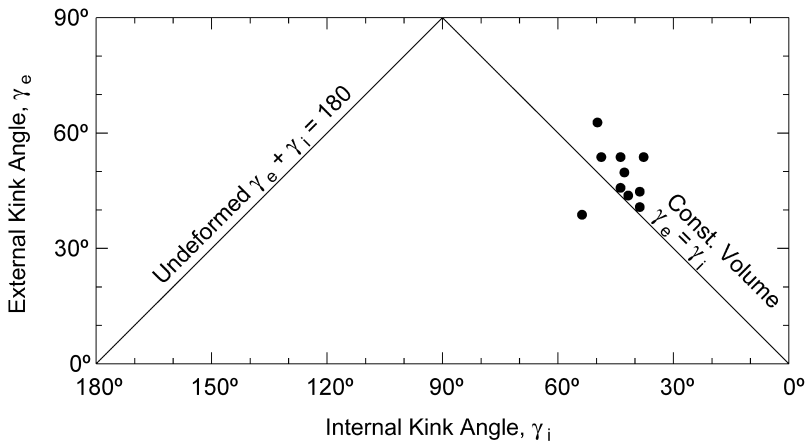

Fig. 8. Diagram showing relationship between external and internal angles of the kink-like subbands in the deformation bands. The triangular area below the lines $\gamma_e + \gamma_i = 180°$ and $\gamma_e = \gamma_i$ indicates that the kink band records an increase in volume during its development, while the area above the line $\gamma_e = \gamma_i$ represents the field of volume decrease within the band (Suppe, 1985).

et al., 1993), suggests that the bands may have arisen from stress concentration in the vicinity of the thrusts.

Deformation bands commonly consist of subbands that represent zones of concentrated deformation. Fig. 11 shows schematically the typical internal structure of the deformation bands. Many of the bands are associated with less steeply dipping subbands that locally displace the boundaries of the deformation bands along slickenlined subband margins, showing a reverse sense with respect to a horizontal plane. On the other hand, some of the subbands are oriented parallel to deformation band boundaries. Regardless of the dips of the subbands, the particle orientation within the subbands is perpendicular to the bedding-parallel phyllosilicate fabric, oriented parallel to the inferred σ_1 direction. Therefore, the subbands within deformation bands are considered to have developed by a combination of flattening perpendicular to σ_1 and shearing along the subband margins. The geometry and kinematic evolution of the subbands are analogous to the S–C bands found in sheared clayey sediments in the décollement zone of the accretionary prism (e.g. Labaume et al., 1997) or in ductile metamorphic rocks (Berthé et al., 1979; Lister and Snoke, 1984). In addition, the internal fabric in subbands may be analogous to compression texture in clay-rich shear zone formed by laboratory deformation study, as the particle orientation within the compression texture is also perpendicular to σ_1 (Tchalenko, 1968). Therefore, our structural analysis of the deformation bands differs from previous works, which asserted that the deformation bands are essentially kink bands (e.g. Lundberg and Moore, 1986) or have a kinematic evolution from kink bands to shear zones (Vannucchi and Tobin, 2000). Since the shearing along the individual subbands consistently shows a reverse sense of shear, the result of the subband-related deformation gives the appearance of kink-like geometry with a reverse asymmetry.

Quantitative physical property analysis using X-ray CT demonstrated a −0.01 to −0.06 porosity reduction associated with the deformation bands (Table 2). However, the subbands cannot be resolved in the CT images because their size is smaller than the theoretical resolution of X-ray CT. Since particles within the subbands are much better oriented than the sectors of the deformation band between the subbands, porosity reduction along the subbands would be greater. Thus, the formation of deformation bands and their subbands would contribute to dewatering of sediments at the toe of the Nankai accretionary prism. Microstructural analysis of deformation bands in the Chile and Costa Rica margins also indicated volume reduction in the deformation bands (Rochford et al., 1995; Vannucchi and Tobin, 2000). Despite differences in the kinematic evolution of the deformation bands between convergent plate margins,

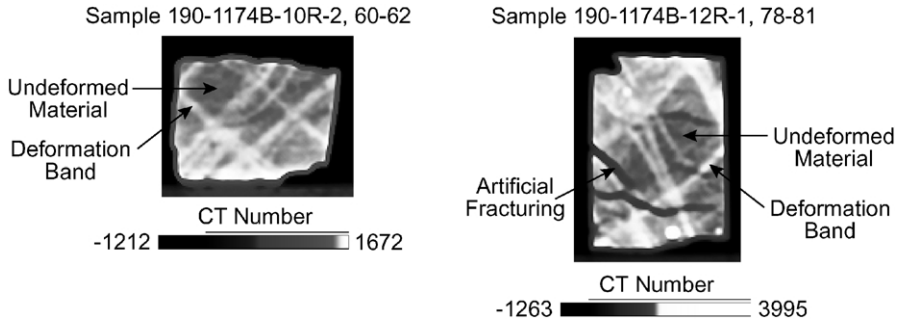

Fig. 9. CT images of deformation bands.

Table 2
Average CT number, average CT number derived bulk density, grain density, and increased bulk density and corresponding porosity reduction in deformation bands relative to surrounding undeformed material

Leg, hole, section, interval (cm)	Average CT number of undeformed material	Standard deviation	Bulk density of undeformed material (g/cm^3)	Average CT number of deformation bands	Standard deviation	Bulk density of deformation bands (g/cm^3)	Bulk density increase in def. bands (g/cm^3)	Grain density (g/cm^3)	Porosity reduction in def. bands
190-1174B-10R-2, 60–62	1449.3	10.78	1.93	1542.1	0	1.99	0.06	2.71	−0.04
190-1174B-10R-2, 60–62	1449.3	10.78	1.93	1520.2	0	1.98	0.05	2.71	−0.03
190-1174B-10R-2, 60–62	1449.3	10.78	1.93	1555.9	10.52	2.00	0.07	2.71	−0.04
190-1174B-10R-2, 60–62	1449.3	10.78	1.93	1561.4	5.49	2.01	0.08	2.71	−0.04
190-1174B-10R-2, 60–62	1449.3	10.78	1.93	1509.2	0	1.97	0.04	2.71	−0.02
190-1174B-11R-1, 21–23	1414.1	6.89	1.91	1507.6	5.27	1.97	0.06	2.65	−0.04
190-1174B-12R-1, 78–81	1348.4	12.59	1.86	1453.6	0	1.93	0.07	2.63	−0.04
190-1174B-12R-1, 78–81	1348.4	12.59	1.86	1449.9	7.32	1.93	0.07	2.63	−0.04
190-1174B-12R-1, 78–81	1348.4	12.59	1.86	1424.3	0	1.91	0.05	2.63	−0.03
190-1174B-12R-1, 78–81	1348.4	12.59	1.86	1409.7	0	1.90	0.04	2.63	−0.03
190-1174B-12R-1, 78–81	1348.4	12.59	1.86	1482.8	0	1.95	0.09	2.63	−0.06
190-1174B-12R-1, 78–81	1348.4	12.59	1.86	1460.9	8.45	1.94	0.08	2.63	−0.05
190-1174B-13R-2, 49–56	1295.5	6.79	1.83	1376.2	5.44	1.88	0.05	2.67	−0.03
190-1174B-13R-2, 49–56	1295.5	6.79	1.83	1384.4	6.28	1.89	0.06	2.67	−0.04
190-1174B-13R-2, 49–56	1295.5	6.79	1.83	1324.6	0	1.85	0.02	2.67	−0.01
190-1174B-13R-2, 49–56	1295.5	6.79	1.83	1408.9	5.44	1.90	0.08	2.67	−0.05
190-1174B-13R-2, 49–56	1295.5	6.79	1.83	1335.5	0	1.86	0.03	2.67	−0.02
190-1174B-13R-2, 49–56	1295.5	6.79	1.83	1368.1	0	1.88	0.05	2.67	−0.03
190-1174B-13R-2, 49–56	1295.5	6.79	1.83	1400.7	0	1.90	0.07	2.67	−0.04
190-1174B-13R-2, 49–56	1295.5	6.79	1.83	1357.2	0	1.87	0.04	2.67	−0.03
190-1174B-15R-CC, 18–24	1299.5	10.9	1.83	1442.7	0	1.93	0.10	2.59	−0.06
190-1174B-15R-CC, 18–24	1299.5	10.9	1.83	1445.4	5.36	1.93	0.10	2.59	−0.06
190-1174B-15R-CC, 18–24	1299.5	10.9	1.83	1365.0	5.36	1.87	0.04	2.59	−0.03
190-1174B-15R-CC, 18–24	1299.5	10.9	1.83	1375.7	5.36	1.88	0.05	2.59	−0.03
190-1174B-15R-CC, 18–24	1299.5	10.9	1.83	1346.2	0	1.86	0.03	2.59	−0.02
190-1174B-15R-CC, 18–24	1299.5	10.9	1.83	1367.6	8.76	1.88	0.05	2.59	−0.03
190-1174B-15R-CC, 18–24	1299.5	10.9	1.83	1399.8	8.76	1.90	0.07	2.59	−0.04
190-1174B-15R-CC, 18–24	1299.5	10.9	1.83	1362.3	6.19	1.87	0.04	2.59	−0.03
190-1174B-15R-CC, 18–24	1299.5	10.9	1.83	1338.1	5.36	1.86	0.03	2.59	−0.02
190-1174B-29R-3, 106–110	1509.2	33.3	1.97	1625.7	5.56	2.05	0.08	2.65	−0.05
190-1174B-39R-4, 30–35[a]	1296.8	5.3	1.83	1325.6	5.25	1.85	0.02	2.66	−0.01
190-1174B-39R-4, 30–35[a]	1296.8	5.3	1.83	1344.0	0	1.86	0.03	2.66	−0.02
190-1174B-39R-4, 30–35[a]	1296.8	5.3	1.83	1372.9	5.25	1.88	0.05	2.66	−0.03
190-1174B-39R-4, 30–35[a]	1296.8	5.3	1.83	1333.5	0	1.85	0.02	2.66	−0.02
190-1174B-39R-4, 30–35[a]	1296.8	5.3	1.83	1344.0	0	1.86	0.03	2.66	−0.02

[a] Ash layer.

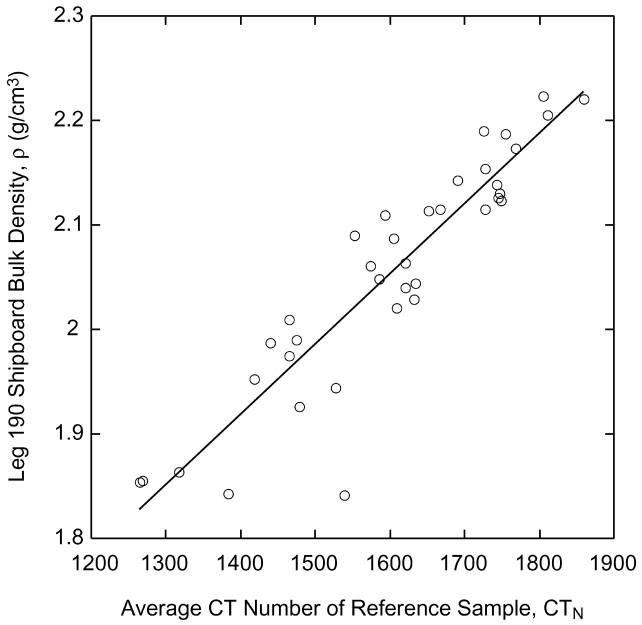

Fig. 10. Diagram showing the relationship between the average CT numbers of the reference samples and Leg 190 shipboard bulk density data. See text for further explanation.

deformation bands play an important role in the drainage of argillaceous sediments.

As σ_1 was inferred to be subhorizontal, the angles between the deformation bands and σ_1 can be more than 45° (Figs. 3 and 4). Maltman et al. (1993) described steeply dipping deformation bands that were spatially associated with less steeply dipping deformation bands. They considered that the steeply and less steeply dipping deformation bands represent Riedel (R_1) and antithetic Riedel (R_2) shears, respectively. However, such close relationships are not seen at Site 1174. Karig and Lundberg (1990) proposed that the deformation bands developed as brittle Coulomb fractures in which the less steeply dipping subbands represent Riedel shears. Deformation bands dipping about 45° to a subhorizontal σ_1 could be consistent with a Coulomb criterion, but bands at angles greater than 45° to the subhorizontal σ_1 are not. Steeply dipping deformation bands may be initially formed at about 45° to the subhorizontal σ_1, and then become passively rotated due to continuous thrusting at the toe of the accretionary prism. However, this possibility is unlikely, because the steeply dipping deformation bands are not associated with tilted bedding or fissility. Alternatively, the deformation bands may have initiated at angles greater than 45° to the subhorizontal σ_1. The results of our structural and physical property analyses indicate that the deformation bands are compactive shear bands. Recent theoretical work indicates that in porous rocks, compacting shear bands develop at angles greater than 45° to σ_1 (Bésuelle, 2001). Ramsay (1980) indicated that the angles between compactive brittle-ductile shear zones and σ_1 could be greater than 45°. Such a steeply oriented displacement may also occur in compactive deformed zones in soft sediments at the toe of an accretionary prism.

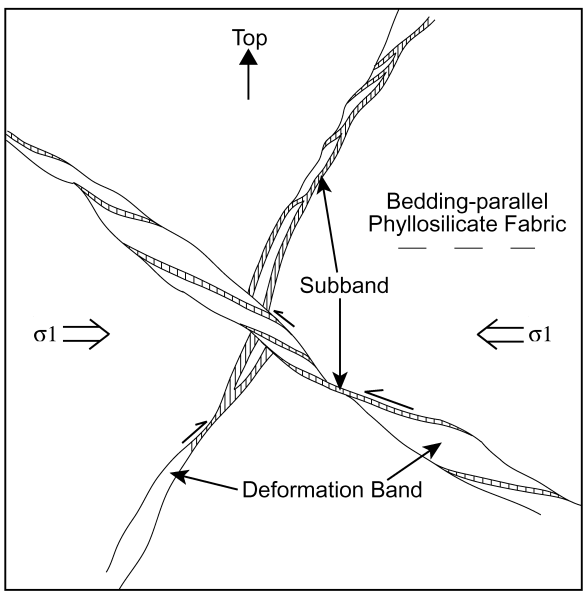

Fig. 11. Schematic diagram showing a representative internal structure of the deformation bands, based on core- and optical microscopic-scale structural analysis. The lines within the subbands indicate the orientation of particles perpendicular to σ_1. Half-arrows indicate sense of shear. Core top is perpendicular to a horizontal plane.

5. Conclusions

The subhorizontal σ_1 associated with northwest-directed plate convergence has produced ~1–10 mm-thick, bedding-oblique deformation bands in argillaceous sediments at the toe of the Nankai accretionary prism. Many of the deformation bands dip between 40 and 70° and typically developed as two oppositely dipping sets. The bands are displaced by the slickenlined surfaces of the oppositely dipping bands, showing a reverse slip with respect to a horizontal plane. Deformation bands commonly consist of thinner and darker subbands that are less steeply dipping or parallel to the boundaries of the deformation bands. A reverse sense of shear with respect to a horizontal plane along the margins of the subbands can be detected by displacement of either the deformation band boundaries or the oppositely dipping subbands. The internal particles in the subbands are oriented perpendicular to σ_1, regardless of the dips of subbands. Quantitative physical property analyses using X-ray CT demonstrate a porosity reduction of −0.01 to −0.06 in the deformation bands relative to the surrounding undeformed material. Therefore, the deformation bands are compactive shear bands, and the subbands arise from a combination of reverse sense of shear and flattening perpendicular to σ_1, with their geometries producing the S–C aspect observed in sheared clayey sediments or ductile metamorphic shear zones.

Acknowledgements

This research used samples and data provided by the Ocean Drilling Program (ODP). ODP is sponsored by the U.S. National Science Foundation and participating countries under the management of the Joint Oceanographic Institutions, Inc. We thank the captain and crew of the *JOIDES Resolution* for their support and cooperation during the cruise. Discussion with Pierre Henry was useful. We thank Hirokuni Oda and Tsukasa Nakano for their assistance in use of the CT scanner. Careful and constructive reviews by Jonathan C. Lewis, Paola Vannucchi, Joao Hippertt, and Gaku Kimura are greatly appreciated.

References

Anderson, S.H., Gantzer, C.J., Boone, J.M., Tully, R.J., 1988. Rapid nondestructive bulk density and soil-water content determination by computed tomography. Soil Science Society of America Journal 52, 35–40.

Berthé, D., Choukroune, P., Jegouzo, P., 1979. Orthogneiss, mylonite and non coaxial deformation of granites: the example of the South Armorican Shear Zone. Journal of Structural Geology 1, 31–42.

Bésuelle, P., 2001. Compacting and dilating shear bands in porous rock: theoretical and experimental conditions. Journal of Geophysical Research 106, 13435–13442.

Byrne, T., Maltman, A., Stephenson, E., Soh, W., Knipe, R., 1993. Deformation structures and fluid flow in the toe region of the Nankai accretionary prism. Proceedings of the Ocean Drilling Program, Scientific Results 131, 83–101.

Karig, D.E., Lundberg, N., 1990. Deformation bands from the toe of the Nankai accretionary prism. Journal of Geophysical Research 95, 9099–9109.

Labaume, P., Maltman, A.J., Bolton, A., Tessier, D., Ogawa, Y., Takizawa, S., 1997. Scaly fabrics in sheared clays from the décollement zone of the Barbados accretionary prism. Proceedings of the Ocean Drilling Program, Scientific Results 156, 59–77.

Lewis, J.C., Byrne, T., Prior, D.J., 1997. Small faults and kink bands in the Nankai accretionary complex: textural observations from Site 808 of ODP Leg 131. The Island Arc 6, 183–196.

Lister, G.S., Snoke, A.W., 1984. S–C mylonites. Journal of Structural Geology 6, 617–638.

Lundberg, N., Moore, J.C., 1986. Macroscoic structural features in Deep Sea Drilling Project cores from forearcs. Geological Society of America Memoir 166, 13–44.

Maltman, A.J., 1998. Deformation structures from the toes of active accretionary prisms. Journal of the Geological Society, London 155, 639–650.

Maltman, A.J., Byrne, T., Karig, D., Lallement, S., 1993. Deformation at the toe of an active accretionary prism: synopsis of results from ODP Leg 131, Nankai, SW Japan. Journal of Structural Geology 15, 949–964.

Moore, G.F., Taira, A., Klaus, A., et al., 2001a. Proceedings of the Ocean Drilling Program, Initial Reports, 190 [CD-ROM]. Available from: Ocean Drilling Program, Texas A&M University, College Station TX 77845-9547, USA.

Moore, G.F., Taira, A., Klaus, A., Becker, L., Boeckel, B., Cragg, B.A., Dean, A., Fergusson, C.A., Henry, P., Hirano, S., Hisamitsu, T., Hunze, S., Kastner, M., Maltman, A.J., Morgan, J.K., Murakami, Y., Saffer, D.M., Sánchez-Gómez, M., Screaton, E.J., Smith, D.C., Spivack, A.J., Steurer, J., Tobin, H.J., Vjiie, K., Underwood, M.B., Wilson, M., 2001b. New insights into deformation and fluid flow processes in the Nankai Trough Accretionary Prism: results of Ocean Drilling Program Leg 190. Geochemistry Geophysics Geosystems, 2:10.1029/2001GC000166.

Nakano, T., Nakashima, Y., Nakamura, K., Ikeda, S., 2000. Observation and analysis of internal structure of rock using X-ray CT. Journal of Geological Society of Japan 106, 363–378.

Ramsay, J.G., 1980. Shear zone geometry: a review. Journal of Structural Geology 2, 83–99.

Rochford, E.L., Prior, D.J., Agar, S.M., Maltman, A., 1995. Microstructural analysis of deformation bands from Site 860, Chile margin. Proceedings of the Ocean Drilling Program, Scientific Results 141, 13–26.

Seno, T., 1977. The instantaneous rotation vector of the Philippine Sea Plate relative to the Eurasian Plate. Tectonophysics 42, 209–226.

Soh, W., Byrne, T., Taira, A., Kono, A., 1993. Computed tomography (CT) scan image analysis of Site 808 cores: Structural and physical property implications. Proceedings of the Ocean Drilling Program, Scientific Results 131, 135–140.

Suppe, J., 1985. Principles of Structural Geology, Prentice-Hall, Englewood Cliffs, New Jersey.

Takizawa, S., Kawata, T., Ohno, Y., 1995. A method of fixation and freeze-drying of soft sediments containing water. Journal of Geological Society of Japan 101, 941–944.

Tchalenko, J.S., 1968. The evolution of kink-bands and the development of compression textures in sheared clays. Tectonophysics 6, 159–174.

Ujiie, K., 1997. Off-scraping accretionary process under the subduction of young oceanic crust: the Shimanto Belt of Okinawa Island, Ryukyu Arc. Tectonics 16, 305–322.

Ujiie, K., Nakano, T., 2002. Physical property analysis of microstructure and the plate boundary décollement zone using X-ray CT. Chikyu Monthly 24, 208–213.

Vannucchi, P., Tobin, H., 2000. Deformation structures and implications for fluid flow at the Costa Rica convergent margin, ODP Sites 1040 and 1043, Leg 170. Journal of Structural Geology 22, 1087–1103.